Colloids and Surfaces A: Physicochemical and Engineering Aspects 676 (2023) 132238

Contents lists available at ScienceDirect

Colloids and Surfaces A: Physicochemical and Engineering Aspects

journal homepage: www.elsevier.com/locate/colsurfa

Ethanol-thermal synthesis of colloidal-CeFeMn mixed-oxide as efficient catalytic material for atmospheric ozone decomposition

Xiao Chen [a,b], Changcheng Zhou [a], Quanli Ke [a], Ying Zhou [a], Xiaomei Zeng [b], Zhunian Jin [b], Huayan Liu [a], Hanfeng Lu [a,*]

[a] Innovation Team of Air Pollution Control, Institute of Catalytic Reaction Engineering, College of Chemical Engineering, Zhejiang University of Technology, Hangzhou 310014, China

[b] Department of Safety and Environmental Protection, Pharmaceutical College, Jinhua Polytechnic, Jinhua 321017, China

HIGHLIGHTS

- Colloidal-CeFeMn mixed-oxide was synthesized by a facile and mild method.
- CeFeMn mixed-oxide with high specific area and abundant oxygen vacancies was successfully synthesized.
- Inert carriers could acquire the ability to eliminate atmospheric O_3 by modification with colloidal-CeFeMn mixed-oxide.

GRAPHICAL ABSTRACT

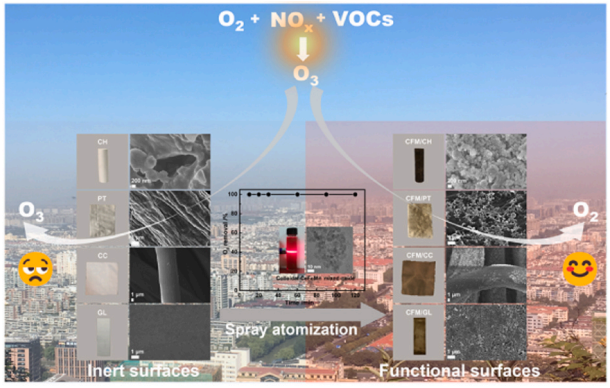

ARTICLE INFO

Keywords:
Atmospheric ozone
Catalytic decomposition
Ethanol-thermal activation
Colloidal-CeFeMn mixed-oxide
Oxygen vacancy

ABSTRACT

Catalytic decomposition of ozone (O_3) shows great potential in eliminating harmful pollutant. However, developing efficient catalysts for atmospheric O_3 remediation remains challenging. To address this problem, we have designed an active dispersion liquid (colloidal-CeFeMn mixed-oxide) for atmospheric O_3 decomposition. The results show that the amorphous CeFeMn mixed-oxide activated at 150 °C has a larger specific surface area and more surface active sites (oxygen vacancies) than those samples activated at 160 °C and 170 °C. It also exhibits superior O_3 decomposition activity at room temperature. Furthermore, ethanol-thermal activation of a CeFeMn-citric acid complex yielded CeFeMn mixed-oxide with small size and high element disorder, resulting in abundant redox pairs and catalytic active sites for O_3 decomposition. With the coverage of the aforementioned colloidal-CeFeMn mixed-oxide, the inert surface of ordinary objects could be easily converted into active surfaces, reducing surrounding O_3 concentration by 20–30 $\mu g \cdot m^{-3}$. This study provides valuable insight into catalyst design and would help to promote the practical application of catalytic decomposition for eliminating atmospheric O_3.

* Corresponding author.
E-mail address: luhf@zjut.edu.cn (H. Lu).

https://doi.org/10.1016/j.colsurfa.2023.132238
Received 24 June 2023; Received in revised form 8 August 2023; Accepted 11 August 2023
Available online 12 August 2023

1. Introduction

Owing to its potent redox activity, excessive O_3 content near the ground can severely damage the ecological environment, causing problems like plant necrosis and reduced crop yields. Additionally, long-term exposure, even to low O_3 levels, poses serious risks to human health and may lead to cardiovascular and respiratory diseases [1–3]. Consequently, the World Health Organization and many countries have implemented strict regulations on atmospheric O_3 levels [4]. Unfortunately, due to industrial development and the widespread use of fossil fuels, O_3 concentration often exceeds these permissible levels [5–7]. Therefore, removing ground-level O_3 is critical for protecting human health and ecosystems. While ozone pollution can theoretically be controlled by reducing VOCs and NO_x emissions, an unbalanced reduction ratio may inadvertently increase O_3 concentration [8–10]. Hence, developing an efficient way to directly purify the atmospheric O_3 remains necessary to address this pressing O_3 pollution issue.

Among the numerous ozone purification methods, catalytic decomposition has attracted substantial attention due to its safety, economy, and efficiency [11–13]. With the deeper understanding of the ozone decomposition mechanism, significant progress has been made in developing highly efficient catalysts that can decompose ozone at ambient temperature [14–18]. Manganese-based oxides, in particular, are considered highly promising catalysts [19–21]. Zhang et al. synthesized a series of spinel (Mn, Co)$_3O_4$ catalysts with abundant active sites (oxygen vacancies) and special surface area using an oxalic coprecipitation method, which displayed excellent catalytic ozonolysis performance [22]. Abdallah et al. developed a novel acid treated Ce_xMn catalyst for O_3 decomposition at low temperature in dry and wet conditions, exhibiting strong water tolerance [23]. Sun et al. reported a new manganese-based metal organic framework (ZZU-281) that catalyzed O_3 decomposition at an almost constant 100 % efficiency across the entire humidity range from dry (≤5 % relative humidity (RH)) to high humidity (90 % RH) [24]. Thus, a rationally engineered manganese-based oxides structure could satisfactorily catalyze O_3 decomposition under various gaseous conditions. However, these synthesized catalysts are normally studied in powder form, which cannot be directly used for atmospheric O_3 remediation. To the best of our knowledge, developing such an effective catalyst for atmospheric ozone decomposition remains a considerable challenge.

The key to catalytic control of atmospheric ozone pollution requires sufficient contact between dispersed ozone in the atmosphere and catalytic materials. This necessitates widely distributing catalytic materials in the environment to increase the probability of contact and collision with ozone. However, traditional solid catalysts used for organized waste gas purification have low feasibility for large-scale deployment in the environment due to morphological restrictions. Therefore, new types of catalytic materials need to be developed to better suit catalytic purification of atmospheric ozone. Our team previously presented a novel strategy for preparing monolithic catalysts, which can facilely and flexibly load active species onto various surfaces [25,26]. According to this strategy, if a highly efficient active dispersion liquid for O_3 decomposition can be synthesized, then simply atomizing and spraying it can generate an active layer on material surfaces in the environment (such as buildings and roads) to capture and decompose O_3 for catalytic purification of atmospheric ozone pollution (Fig. 1a).

In this work, we propose a facile and mild preparation strategy to manufacture colloidal-CeFeMn mixed-oxide (Fig. 1b). Experimental results confirm that the stable colloidal solution consists of CeFeMn mixed-oxides with abundant oxygen vacancies and ultra-high specific surface area, which can be readily combined with diverse solids to form catalytic materials. These materials exhibited satisfactory O_3 removal efficiency under various experimental conditions.

2. Material and methods

2.1. Catalyst synthesis

1.28 mmol of $Mn(NO_3)_2$, 0.64 mmol of $Fe(NO_3)_3$, 0.08 mmol of $Ce(NO_3)_3$, 2 mmol of citric acid and 3×10^{-3} g of sodium hexametaphosphate were dissolved in 10 ml of deionized water. The solution was stirred at 90 °C for 1 h to form CeFeMn-citric acid complex. After cooling, 10 ml of ethanol was added while stirring for 10 min. The mixed solution was transferred to a 25 ml crystallization kettle and activated at 140 °C, 150 °C, 160 °C, or 170 °C for 1 h. After cooling and centrifugation, the solid product was either dried naturally to obtain CeFeMn mixed-oxide (CFM) powder (Fig. S1) or dispersed in ethanol to obtain colloidal-CeFeMn mixed-oxide (Fig. 1b). The CFM samples activated at different temperatures were denoted as CFM-140, CFM-150, CFM-160, and CFM-170 respectively.

2.2. Catalyst characterization

Thermogravimetric (TG) analysis was performed using a Netzsch STA 409PC. Fourier transform infrared (FTIR) spectroscopy (Vertex 70, Bruker Optics, Germany) was used to examine infrared spectra. X-ray diffraction (XRD) patterns were collected using an X-ray diffractometer (PANalytical X'Pert PRO, $\lambda = 0.1542$ nm). X-ray photoelectron spectroscopy (XPS) was carried out on a Kratos AXIS Ultra DLD spectrometer to identify valence states and surface composition. N_2 adsorption-desorption isotherms were obtained at 77 K using a Micromeritics ASAP2020 instrument. Scanning electron microscopy (SEM) images were acquired using a Hitachi S-4700(II) microscope at 15.0 kV. Transmission electron microscopy (TEM) images were taken with a

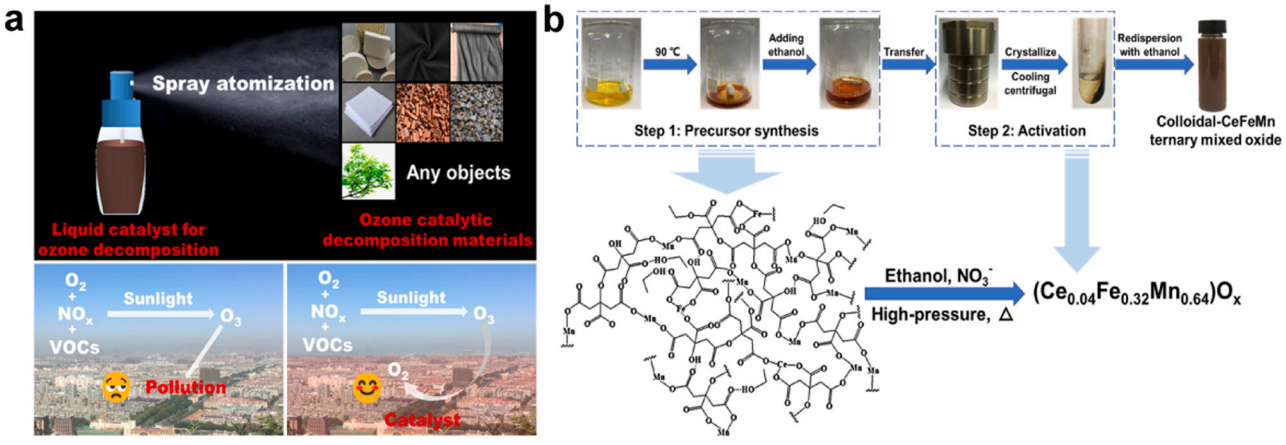

Fig. 1. Scheme of (a) O_3 pollution control by catalytic technology and (b) colloidal-CeFeMn mixed-oxide.

Tecnai F30 S-Twin microscope at 300 kV. UV spectra were recorded on a Shimadzu UV-2600 spectrometer. H_2 temperature-programmed reduction (H_2-TPR) was performed using a FINE SORB-3010 E instrument equipped with a thermal conductivity detector (TCD). O_2-Temperature programmed desorption (O_2-TPD) was conducted on a BelCata II instrument equipped with an online QIC-200 quadrupole mass spectrometer. Raman spectra were obtained using a Raman spectrometer (HR 800 Lab RAM, Horiba Jobin Yvon, France) equipped with a 531.95 nm laser (frequency-doubled Nd:YAG, 20 mW). Electron paramagnetic resonance (EPR) spectra were recorded on a Bruker EMX plus 10/12 spectrometer (X-band, 9.84 GHz, 2 mW, 100 kHz modulation).

2.3. Catalyst evaluation

Catalyst performance for organized ozone decomposition was evaluated in a continuous fixed-bed reactor at 25 °C. Ozone was generated by passing dry oxygen through an ozone generator (COM-AD-01-OEM, Anseros Company, Germany) and was adequately mixed with clean air to maintain a 60 ppm concentration. The inlet and outlet ozone concentration were monitored using an ozone detector (Model 106-M, 2B Technologies Inc., USA).

3. Results and discussion

3.1. Formation of active CeFeMn mixed-oxide

Fig. 2 shows the catalytic activities for O_3 decomposition of all powder samples to evaluate the performance of CeFeMn mixed-oxide synthesized by ethanol-thermal activation at different temperatures. Notably, the activity of sample activated at 140 °C was significantly lower than that the other samples. This is potentially attributed to incomplete decomposition of the CeFeMn-citric acid complex, resulting in a reduced formation of more active oxides. As the ethanol-thermal temperature increased, the catalytic activity of the sample improved. However, excessively high temperatures appear to have a counterproductive effect on the activity of CeFeMn mixed-oxide. To understand the specific reasons for the variability in activity of CeFeMn mixed-oxide synthesized at different ethanol-thermal temperatures, a series of characterizations were carried out.

Thermogravimetric analysis and infrared spectroscopy were employed to investigate the decomposition of the CeFeMn-citric acid complex at different ethanol-thermal temperatures. The outcomes are demonstrated in Fig. 3. Fig. 3a shows the TG and DTG curves of the CeFeMn-citric acid complex and its ethanol-thermal products at

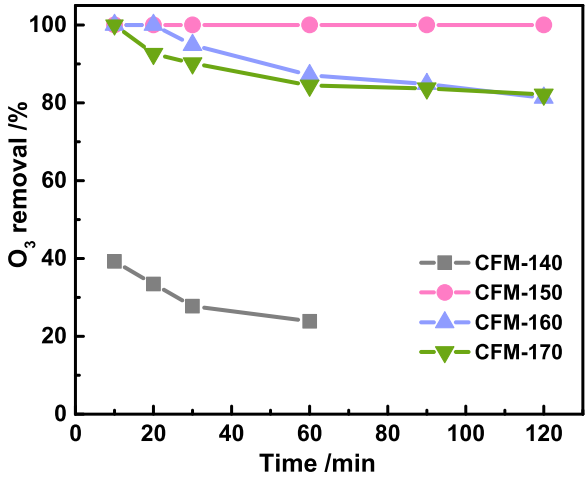

Fig. 2. O_3 conversion on CeFeMn mixed-oxide powder prepared at different ethanol-thermal temperatures. Reaction conditions: ~60 ppm O_3, WHSV = 600,000 ml·g^{-1}·h^{-1}, 25 °C, dry gas.

different temperatures. It is evident that the weight loss of CeFeMn-citric acid complex mainly occurred in three stages: the first stage below 180 °C represents desorption of physically adsorbed water, chemically adsorbed water, and volatile components on the sample surface [27]; the second stage from 180 °C to 300 °C corresponds to decomposition of nitrates, hydroxides, and hydrated oxides in the sample [28]; the third stage between 300 °C and 360 °C results from decomposition of CeFeMn-citric acid complex [29,30]. Two weight loss peaks appear in the DTG curve at 300–360 °C, corresponding to decomposition of CeFeMn-citric acid complex with different coordination forms (monodentate coordination or bidentate coordination). Based on the thermogravimetric analysis of CeFeMn-citric acid complex, the sample activated at 140 °C lacked a weight loss peak at 300–360 °C, likely due to decomposition of a certain coordination form of the complex caused by the 140 °C ethanol-thermal treatment. Furthermore, the newly added fourth stage of weight loss from 360 °C to 450 °C can be attributed to decomposition of esters [31], potentially due to esterification between some citrate ions and ethanol at 140 °C. Combined with the infrared spectrum (Fig. 3b), only a small amount of citrate decomposed at 140 °C, failing to produce substantial active oxides. For samples activated at 150 °C, 160 °C and 170 °C, almost no weight loss occurred above 300 °C (Fig. 3a), and the N-O vibration characteristic peak of nitrate at 1380 cm^{-1} and C═O vibration characteristic band of citrate at 1000 cm^{-1} [32–34] significantly weaken (Fig. 3b), indicating that the complex is almost fully decomposed. Additionally, it is noteworthy that these samples exhibited weight increase above 750 °C (Fig. 3a), signifying abundant oxygen vacancies.

XRD and N_2 adsorption-desorption were used to evaluate the texture properties of CeFeMn mixed-oxide activated at 150 °C, 160 °C, and 170 °C. The XRD patterns (Fig. 4a) show that the crystal phase of the prepared samples was Bixbyite Mn_2O_3, with no related diffraction peaks of Fe and Ce species observed. This could indicate that Ce and Fe entered the lattice of Mn_2O_3 in a highly disordered manner, resulting in lower crystallinity for the samples. Among them, CFM-150 showed an amorphous structure, implying that abundant surface defects (such as oxygen vacancies) were present, which is conducive to oxygen migration. With increasing activation temperature, the crystallinity of the synthesized samples gradually increased. For instance, CFM-160 began to exhibit an obvious Mn_2O_3 crystalline phase. When the activation temperature was further increased to 170 °C, the synthesized sample still maintained the Mn_2O_3 crystalline phase. However, the structure became more complex due to the enhanced reducibility of ethanol, leading to decreased XRD peak intensity. The adsorption-desorption isotherms and BJH pore size distribution curves are illustrated in Fig. 4b-d. The isotherms of all samples belonged to type IV with a small H3 hysteresis loop. Pore size distributions show a broad peak centered at 4–5 nm, indicating that the ethanol-thermal products were small in size, as confirmed by the high specific surface area of all samples. The specific surface area of CFM-150, CFM-160, and CFM-170 calculated by the Brunauer-Emmett-Teller (BET) method was 372 $m^2 \cdot g^{-1}$, 313 $m^2 \cdot g^{-1}$, and 292 $m^2 \cdot g^{-1}$ respectively. With increasing activation temperature, the crystallinity of the particles increased, resulting in decreased specific surface area. In summary, XRD and BET results demonstrate that CFM-150 possesses a more favorable physical structure (abundant defects and large specific surface area) for catalyzing ozone decomposition.

Based on the analysis of the above characterization, the hypothesized mechanism of ethanol-thermal synthesis of CeFeMn mixed-oxide is illustrated in Fig. 5. Metal ions (Mn^{2+}, Fe^{3+} and Ce^{3+}) could form complexes with citric acid and undergo polymerization to form chain structures at certain temperatures. Upon introduction of ethanol, hydroxyl and carboxyl groups could undergo condensation, promoting the formation of a polymer network structure. Under increasing temperature and pressure conditions during ethanol-thermal synthesis, the polymer decomposed and was oxidized by nitrate, ultimately generating an oxide active structure. Thanks to the uniform dispersion of metal ions (Mn^{2+}, Fe^{3+} and Ce^{3+}) in the polymer grid through the action of citric

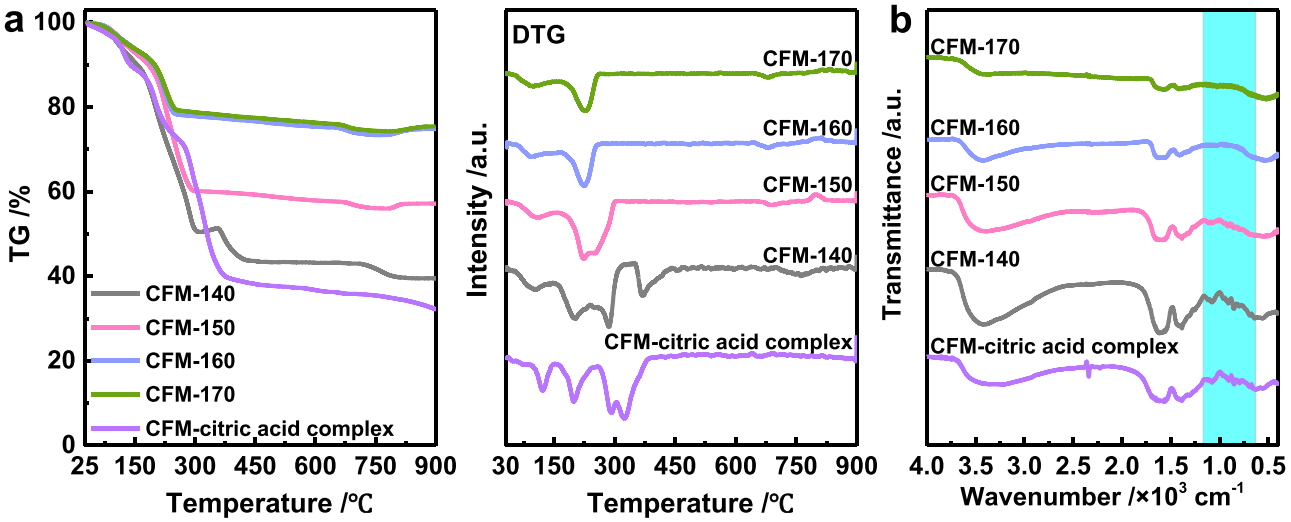

Fig. 3. (a) Thermogravimetric curves under flowing air and (b) infrared spectrum of CeFeMn-citric acid complex and CeFeMn mixed-oxide powder prepared at different ethanol-thermal temperatures.

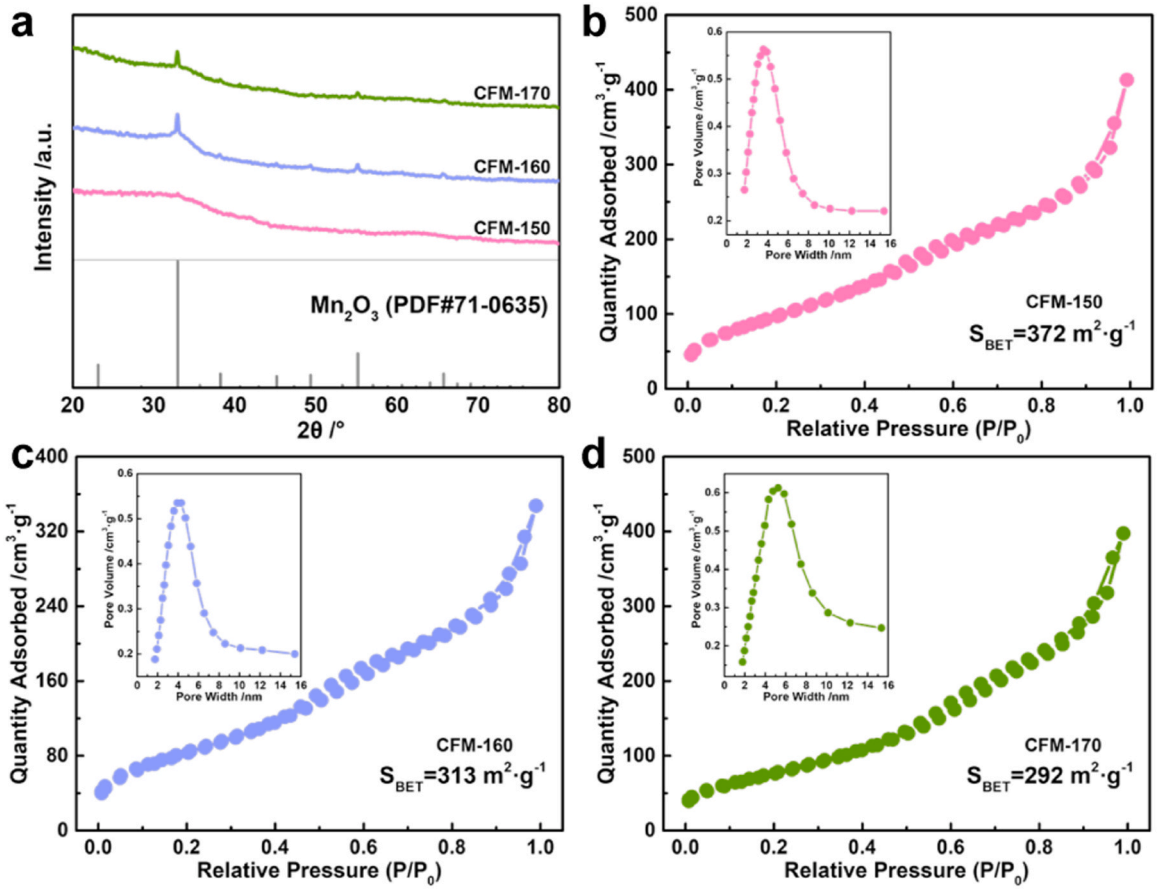

Fig. 4. (a) XRD patterns (b-d) N_2 adsorption-desorption isotherms and pore size distribution curves of CeFeMn mixed-oxide powder prepared at different ethanol-thermal temperatures.

acid and ethanol, the resulting composite oxide primarily exhibited a single manganese oxide (Mn_2O_3) phase. Due to the blocking effects of solvents and surfactants, the resulting particle size was small and exhibited a large specific surface area. Therefore, it can be concluded that the ethanol-thermal synthesis of active oxides for catalytic O_3 decomposition is feasible.

XPS spectra were used to investigate the surface physicochemical properties of CeFeMn mixed-oxide synthesized by ethanol-thermal activation. In Fig. 6a, the Mn $2p_{3/2}$ and Fe $2p_{3/2}$ XPS spectra for all samples are presented. Mn^{2+} (640.6 eV), Mn^{3+} (641.9 eV), Mn^{4+} (643.7 eV), Fe^{2+} (710 eV), Fe^{3+} (711 eV) and Fe^{4+} (713 eV) were detected on the surface of all samples and are listed in Table 1. Previous

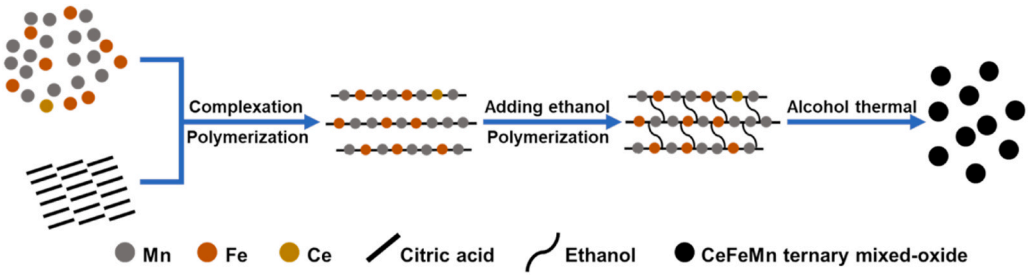

Fig. 5. Ethanol-thermal synthesis mechanism of CeFeMn mixed-oxide.

studies have indicated that the mixed valence state of metal elements in transition metal oxides significantly influences electron transfer during reactions [35–37]. Generally, oxides with a higher content of the intermediate valence state of the variable-valence metal, resulting in more $M^{(n-1)+}/M^{n+}$ and $M^{n+}/M^{(n+1)+}$ redox pairs, are more likely to generate oxygen vacancies. Combined with the relative content of O_{latt} (529.6 eV), O_{vac} (531.3 eV) and O_{surf} (532.1 eV) in the O 1 s XPS spectra (Fig. 6b and Table 1), it is evident that CFM-150 has abundant oxygen vacancies. This finding is further confirmed by Raman, H_2-TPR, and O_2-TPD, as shown in Fig. S2. As the activation temperature increased, due to the disproportionation reaction of Mn^{3+} [38], the content of Mn^{3+} in the CFM-160 sample decreased, while the content of Mn^{2+} and Mn^{4+} increased compared to the CFM-150 sample. However, when the activation temperature further increased, under the reduction by ethanol, Mn^{4+} and Mn^{3+} were reduced. Therefore, compared to the CFM-160 sample, the content of Mn^{4+} in the CFM-170 sample decreased, while the content of Mn^{2+} and Mn^{3+} increased. XPS results demonstrate that the order of oxygen vacancy content in samples synthesized at different ethanol-thermal temperatures is: CFM-150 >CFM-170 >CFM-160. This was confirmed by the intensity of the symmetric EPR signal at g = 2.003 (Fig. 6c). Combined with the specific surface area, it can be concluded that among all samples, CFM-150 has the best catalytic ozone decomposition activity, corroborated by the activity test results (Fig. 2). Although CFM-160 had a lower oxygen vacancy concentration, its specific surface area (313 $m^2 \cdot g^{-1}$) was higher than that of CFM-170 (292 $m^2 \cdot g^{-1}$). Therefore, the oxygen vacancies over CFM-160 may be more easily approached by ozone, which is also consistent with the activity test results.

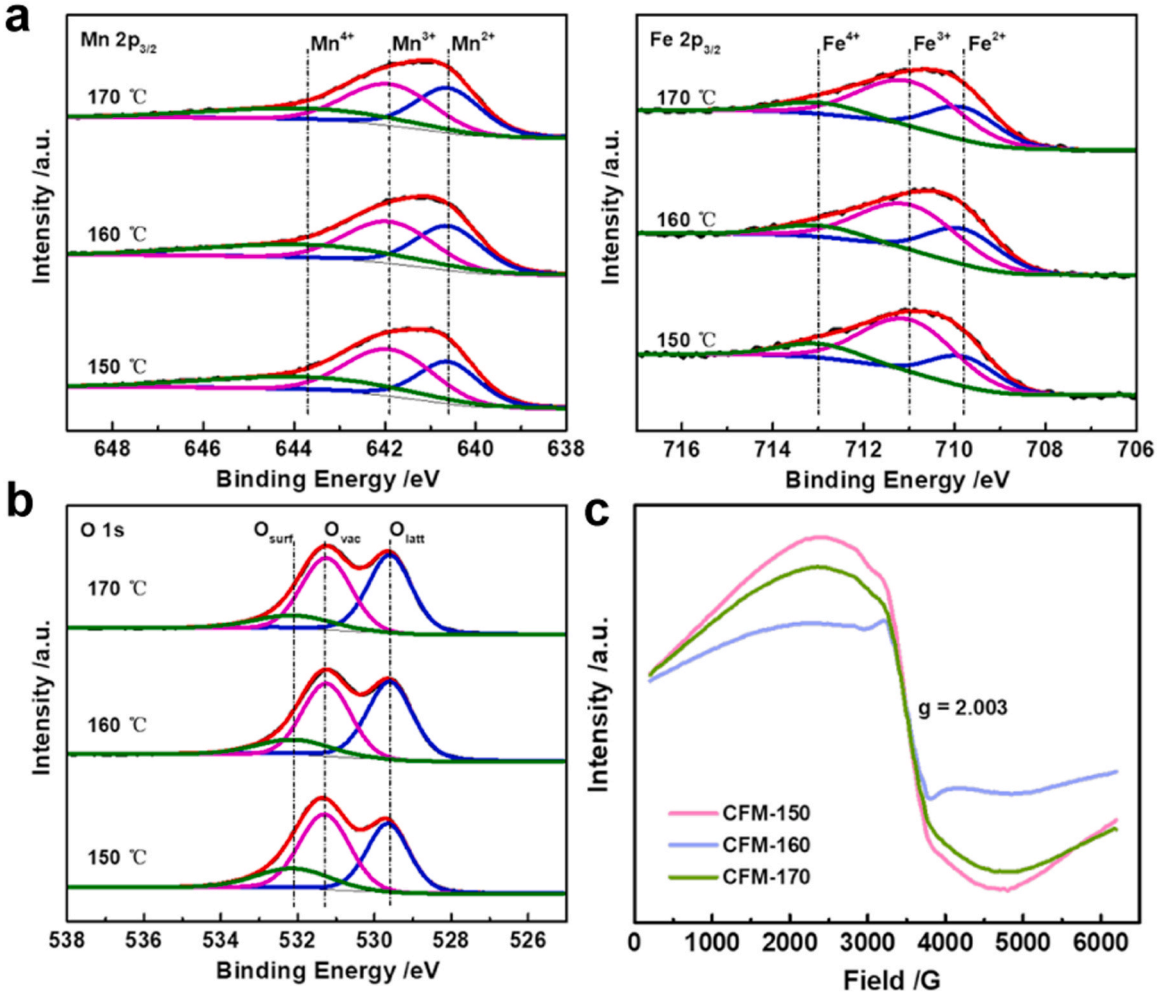

Fig. 6. (a) Mn $2p_{3/2}$ and Fe $2p_{3/2}$, (b) O 1 s XPS spectra and (c) EPR profile of CeFeMn mixed-oxide powder prepared at different ethanol-thermal temperatures.

Table 1
XPS results of CeFeMn mixed-oxide powder prepared at different ethanol-thermal temperatures.

Ethanol-thermal temperatures /°C	Mn (%)			Fe (%)			O (%)		
	Mn^{2+}	Mn^{3+}	Mn^{4+}	Fe^{2+}	Fe^{3+}	Fe^{4+}	O_{latt}	O_{vac}	O_{surf}
150	30.9	42.6	26.5	24.7	61.7	13.6	37.8	45.1	17.1
160	33.9	38.1	28.0	32.0	56.4	11.6	46.3	40.9	12.8
170	36.5	40.2	23.3	29.4	58.3	12.3	45.5	42.6	11.9

3.2. *Colloidal-CeFeMn mixed-oxide and its stability*

The foregoing discussion has demonstrated the successful synthesis of active CeFeMn mixed-oxide through the ethanol-thermal activation of CeFeMn-citric acid complex. The crucial factor in achieving our idea of efficient decomposition of environmental O_3 (Fig. 1a) is determining whether these oxides can form a stable colloidal solution. Fig. 7a exhibits the photos of the CeFeMn mixed-oxide (activated at 150 °C) dispersed in ethanol. The obvious Tyndall effect indicates that the CeFeMn mixed-oxide was uniformly dispersed in the ethanol solvent. Furthermore, transmission electron microscopy (Fig. 7b) reveals clearly defined boundaries separating the nanoparticles (approximately 5 nm), with no observed agglomeration. This can be explained by the following facts: the mechanism of the dispersant, sodium hexametaphosphate (added in the preparation process), is to form a stable double-layer structure on the surface of particles. First, the surface of the particles preferentially adsorbs ions of a certain charge type (determined by the nature of particles) from the dissociation of the dispersant. Then it assembles another type of ions on the surface close to these ions to achieve charge balance. The presence of an ion layer with the same charge on the particle surface leads to particles repelling each other, thereby effectively preventing the aggregation of nanoparticles in ethanol. As a result, a highly dispersed colloidal solution (colloidal-CeFeMn mixed-oxide) is obtained. The TEM-mapping (50 nm) and SEM-mapping (700 nm) are given in Fig. 7c and S3, respectively. Ce, Fe and Mn species were uniformly distributed at different scales, directly indicating the formation of a highly disordered composite structure, which aligns with our speculation (Figs. 4a and 5).

Stability is one of the important parameters for determining the practical application potential of colloidal-CeFeMn mixed-oxide. Therefore, the stability of colloidal-CeFeMn mixed-oxide (activated at 150 °C) was evaluated, with results shown in Fig. 8. The dispersion stability of colloidal-CeFeMn mixed-oxide was judged by its appearance (Fig. 8a). Observing the sample stored for 1 h, 1 d, 7 d, 15 d and 30 d shows that the dispersion state and transparency after storage were the same as those of the fresh sample, with no significant changes observed. Further, the dispersion stability was evaluated by UV characterization (Fig. 8b). The UV spectra obtained from the sample stored at varying times demonstrate consistency, indicating that the dispersion of colloidal-CeFeMn mixed-oxide remained unchanged over time. To explore the effect of long-term storage of colloidal-CeFeMn mixed-oxide on its catalytic performance for ozone decomposition, we conducted activity tests on the post-storage sample powder under high space velocity conditions (ensuring conversion rate < 100 %). Results in Fig. 8c show that the activity and stability of fresh colloidal-CeFeMn mixed-oxide improved after storage, stabilizing after 1 d of aging. This suggests that some reactions occur in CeFeMn mixed-oxide nanoparticles dispersed in ethanol, forming a stable CeFeMn mixed-oxide active

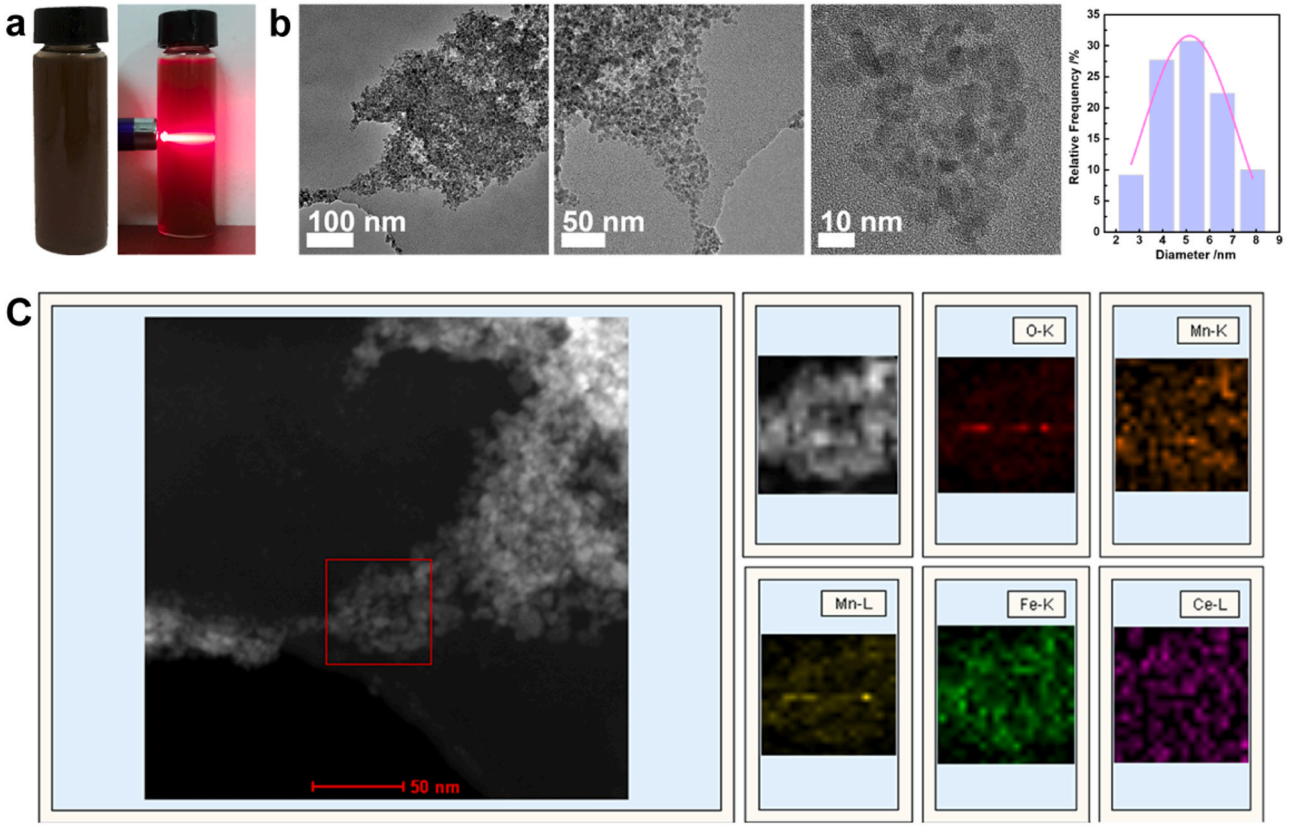

Fig. 7. (**a**) Photograph and tyndall effect, (**b**) TEM images and (**c**) STEM-HAADF images of colloidal-CeFeMn mixed-oxide.

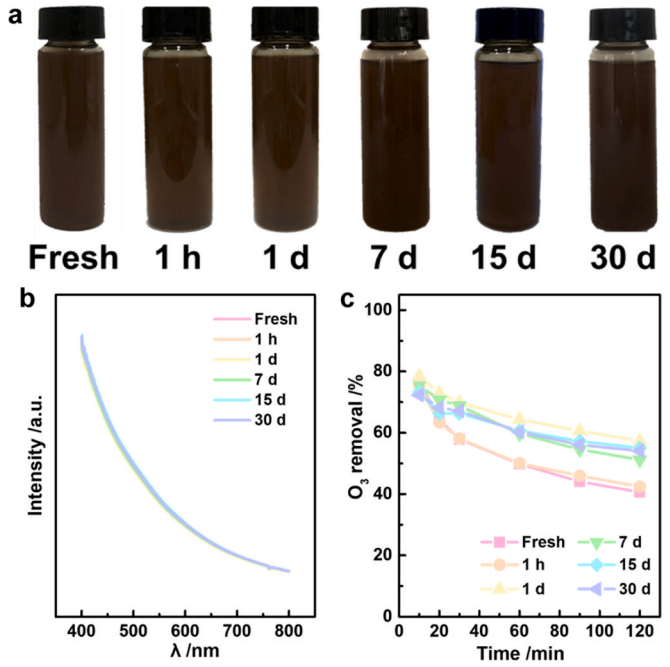

Fig. 8. (a) Photograph, (b) UV spectra and (c) O_3 conversion of colloidal-CeFeMn mixed-oxide in different store time. Reaction conditions: ~60 ppm O_3, WHSV = 12,000,000 ml·g^{-1}·h^{-1}, 25 °C, dry gas.

structure after a period of time. Notably, this change is beneficial for practical applications. These results indicate that colloidal-CeFeMn mixed-oxide can be stored long-term. They also denote that a robust colloidal solution, designed for decomposing environmental O_3, can be effectively synthesized using the approach outlined in Fig. 1b.

3.3. Functional modification of inert carriers

From the above discussion, the desired active dispersion liquid for O_3 decomposition has been successfully synthesized. Cordierite honeycomb (CH), cotton cloth (CC), paper towel (PT) and glass (GL) were selected as catalyst carriers. The colloidal-CeFeMn mixed-oxide (activated at 150 °C) was sprayed by atomization onto the surface of these objects to prepare CFM/CH, CFM/CC, CFM/PT, and CFM/GL catalytic materials. Observation of the blank carriers and catalytic materials by naked eye and scanning electron microscopy (SEM) shows that following colloidal-CeFeMn mixed-oxide spraying by atomization, each carrier was coated with a layer of active nanoparticles on its exterior (Fig. 9). Therefore, the otherwise inert surface of an object can acquire the capability to catalyze O_3 decomposition through application of colloidal-CeFeMn mixed-oxide.

Fig. 10 shows the adhesion and activity of CeFeMn mixed-oxide on different carriers. According to data presented in Fig. 10a, following 30 min of ultrasonic vibration, the weight loss rate of CFM/GL was 1.44%, while the weight loss rate of other samples remained below 1%. These results suggest that the active nanoparticles can be effectively and durably affixed onto the carrier surface, particularly those with roughness. According to the activity test results in Fig. S4, the four carriers could not facilitate O_3 decomposition at ambient temperature. After application of colloidal-CeFeMn mixed-oxide, the carriers exhibited outstanding efficacy in catalytic O_3 decomposition (Fig. 10b). Notably, the reaction rates of the four catalytic materials remained above 3.5×10^{-3} mol·g^{-1}·h^{-1} after 3 h operation, even at high space velocity ($> 1.8 \times 10^{6}$ ml·g^{-1}·h^{-1}). This places them in the upstream range of reported O_3 decomposition catalysts (Table 2). To evaluate the catalytic decomposition ability of colloidal-CeFeMn mixed-oxide for highly dispersed ozone in space, measuring devices and catalytic materials were designed as shown in Figs. S5 and S6. According to the findings (Fig. S7), the object surface modified with colloidal-CeFeMn mixed-oxide obtained the ability for ambient catalytic decomposition of highly dispersed O_3 in space, and the larger the area of the modified object, the stronger the catalytic ability. These results imply that the idea (Fig. 1a) of endowing any object with catalytic ability through active dispersion liquid for O_3 decomposition is feasible.

To further evaluate the room-temperature catalytic ozone decomposition ability of the object surface modified by colloidal-CeFeMn mixed-oxide, we took CFM/CH (CFM loading 2 %) as an example and investigated its activity changes under different humidity conditions.

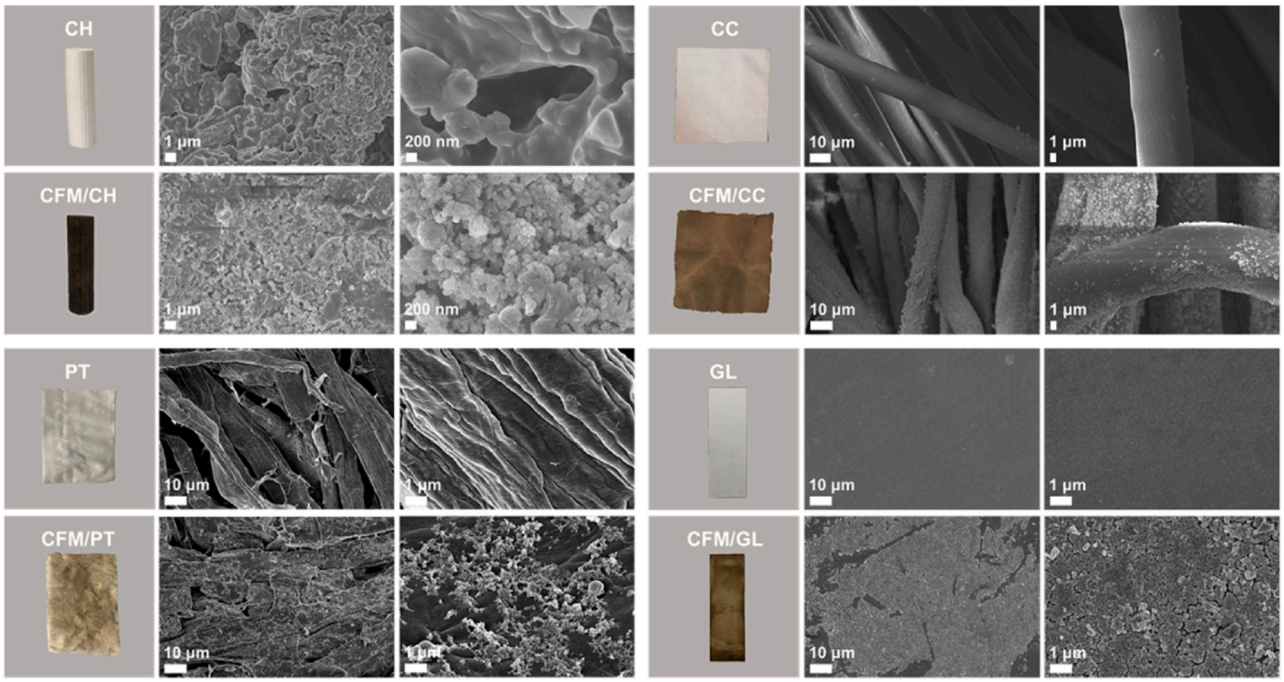

Fig. 9. Photograph and SEM images of carriers and CeFeMn mixed-oxide monolithic catalysts.

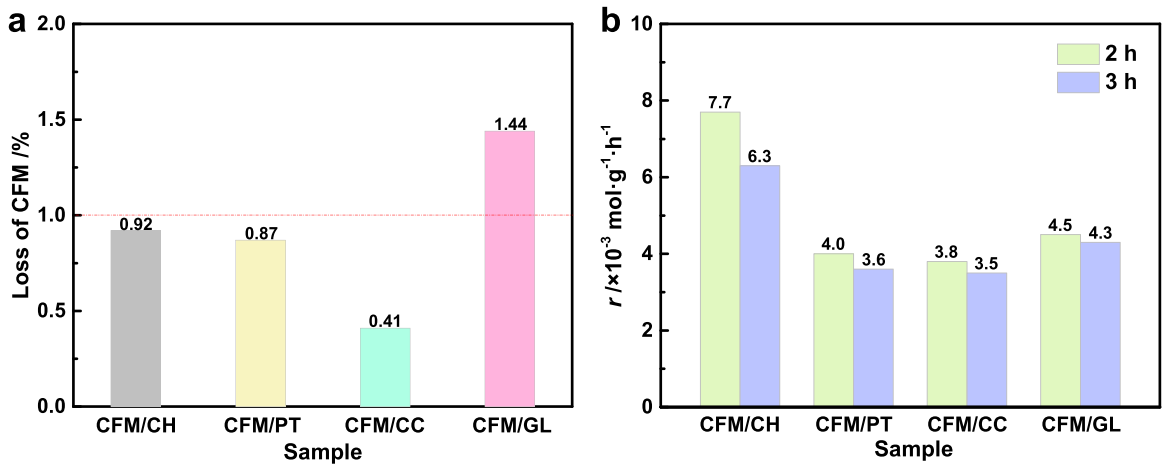

Fig. 10. (**a**) Loss of active components on the CeFeMn mixed-oxide monolithic catalysts after ultrasonic vibration., (**b**) O_3 catalytic decomposition rate on the CeFeMn mixed-oxide monolithic catalysts; reaction conditions: ~60 ppm O_3, 25 °C, dry gas.

Table 2
O_3 catalytic decomposition rate over different catalysts (dry gas).

Sample	O_3 /ppm	Temperature /°C	Space velocity	Reaction time /h	Reaction rate /× 10^{-3} mol·g^{-1}·h^{-1}	Ref.
Ce-γ-MnO_2(pH=7)	40	30	2 × 10^6 h^{-1}	2	7.8	[39]
Co-MnO_x (0.36) /Al	1000	25	7.2 × 10^4 ml·g^{-1}·h^{-1}	3	5.5	[40]
Ni-MnO_x/DE	13	40	2.5 × 10^5 h^{-1}	3	0.5	[41]
Ce-MnO_2(0.28)	60	25	1.2 × 10^6 ml·g^{-1}·h^{-1}	3	2.4	[42]
Ag/Al_2O_3	20,000	-	6 × 10^3 ml·g^{-1}·h^{-1}	3	5.3	[43]
CFM/CH	60	25	6 × 10^6 ml·g^{-1}·h^{-1}	2	7.7	This work
				3	6.3	
CFM/PT			2.2 × 10^6 ml·g^{-1}·h^{-1}	2	4.0	
				3	3.6	
CFM/CC			2 × 10^6 ml·g^{-1}·h^{-1}	2	3.8	
				3	3.5	
CFM/GL			1.8 × 10^6 ml·g^{-1}·h^{-1}	2	4.5	
				3	4.3	

This was compared with a commercial ozone decomposition catalyst (COC, main components 95.06 % C, 1.39 % Mn, 0.82 % Fe, 0.78 % Na, 0.37 % Al, 0.21 % Mg, 0.13 % S by XRF detection), shown in Fig. 11. After 10 h in a 60 % relative humidity gas stream, the activity of COC began declining with ozone conversion dropping to about 80 % after a 20 h reaction. Ozone conversion over CFM/CH remained stable above 95 % during this period. When humidity was reduced to 40 % for 10 h, the ozone conversion over CFM/CH remained above 95 %, while that over the COC remained around 80 %. When humidity increased to 90 % for 10 h, CFM/CH showed some deactivation but ozone conversion still reached over 90 %, while COC dropped to about 60 %. When humidity was reduced to 0 %, CFM/CH activity quickly recovered, with 100 % ozone conversion after another 5 h, but COC activity could not fully recover. These results indicate that the CFM layer on the object surface has excellent catalytic activity, stability and water resistance, adapting to different atmospheric humidity environments.

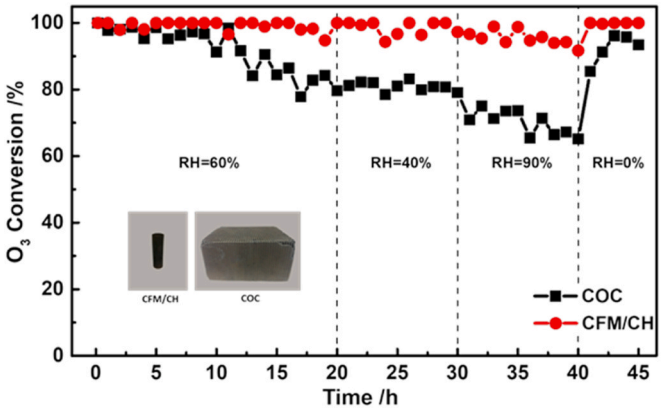

Fig. 11. Comparison of catalytic ozone decomposition performance of CFM/CH and COC under different relative humidity conditions; Reaction conditions: ~60 ppm O_3, GHSV = 6000 h^{-1}, 25 °C.

3.4. *Evaluating the ability to catalyze atmospheric O_3 decomposition*

To further evaluate the potential utility of colloidal-CeFeMn mixed-oxide for catalyzing atmospheric O_3 decomposition, a simulation experiment was undertaken (Fig. 12). Utilizing the device depicted in Fig. S5, we opened the gas box without ozone introduction to directly connect with the atmosphere. The atmospheric O_3 concentration within the box was observed in real-time as the CFM/SS (colloidal-CeFeMn mixed-oxide sprayed by atomization on sunscreen surface) was alternatively inserted or withdrawn. As per the monitoring data analysis, an overall ascending trend was observed in O_3 concentration over time, correlating with the typical pattern of atmospheric O_3 concentration change. However, the ozone concentration in the box with CFM/SS was 20–30 μg·m^{-3} lower than without CFM/SS. This provides evidence that using colloidal-CeFeMn mixed-oxide can facilitate atmospheric ozone decomposition at ambient temperature, aligning with the hypothesis in Fig. 1a.

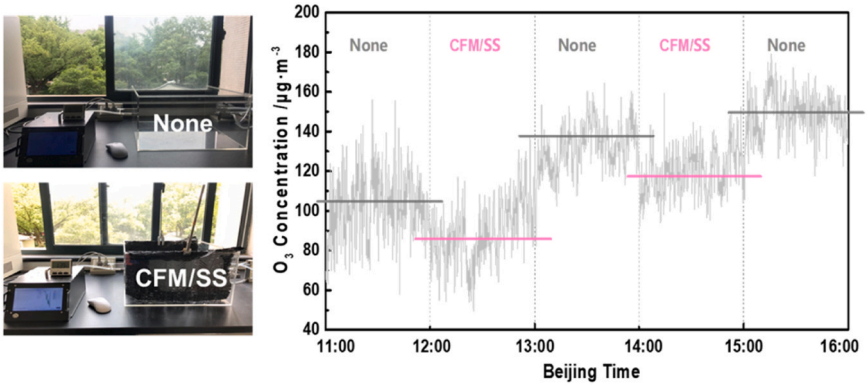

Fig. 12. CFM/SS catalytic decomposition of atmospheric ozone test.

4. Conclusions

In brief, our study has presented a mild and simple ethanol-thermal synthesis technique for creating colloidal-CeFeMn mixed-oxide. A range of characterizations indicate that the synthesized CeFeMn mixed-oxides possess notable features, such as considerable specific surface area and abundant oxygen vacancies, making them promising for catalytic O_3 decomposition. Notably, the sample synthesized at 150 °C exhibits exemplary catalytic activity. Moreover, ordinary objects could be transformed into highly effective materials for catalytic O_3 decomposition when combined with the colloidal-CeFeMn mixed-oxide. This offers a viable solution for preventing and managing atmospheric O_3 pollution through catalytic technology, as attested by the data (20–30 μg·m^{-3} lower atmospheric O_3 concentration) from the simulation experiment. The information acquired in this work lays the groundwork for mitigating atmospheric O_3 at ambient temperature while providing valuable insights for developing highly efficient catalysts for atmospheric O_3 decomposition in the future.

CRediT authorship contribution statement

H.F.L. and X.C. conceived the project. X.C., C.C.Z. and H.F.L. designed the experiments. X.C. and C.C.Z. prepared the samples and performed the experiments. Q.L.K. and Y.Z. characterized the samples. X.C., C.C.Z., Q.L.K., Y.Z., X.M.Z. and H.F.L. analyzed the data and discussed the results. X.C. wrote the manuscript. H.F.L., Z.N.J. and H.Y.L. edited the manuscript. H.F.L. and H.Y.L. guided and supervised the project. All authors contributed to the final manuscript.

Declaration of Competing Interest

The authors declare that they have no known competing financial interests or personal relationships that could have appeared to influence the work reported in this paper.

Data availability

Data will be made available on request.

Acknowledgments

This work was supported by the National Natural Science Foundation of China (No. 22078294), Zhejiang Provincial Natural Science Foundation of China (LZ21E080001, LGF20E080018) and Jinhua Science and Technology Bureau (2022–4-006).

Appendix A. Supporting information

Supplementary data associated with this article can be found in the online version at doi:10.1016/j.colsurfa.2023.132238.

References

[1] E. Paoletti, Z.Z. Feng, A.D. Marco, Y. Hoshika, H. Harmens, E. Agathokleous, M. Domingos, G. Mills, P. Sicard, L. Zhang, E. Carrari, Challenges, gaps and opportunities in investigating the interactions of ozone pollution and plant ecosystems, Sci. Total Environ. 709 (2020), 136188, https://doi.org/10.1016/j.scitotenv.2019.136188.

[2] M. Namdari, C.S. Lee, F. Haghighat, Active ozone removal technologies for a safe indoor environment: a comprehensive review, Build. Environ. 187 (2021), 107370, https://doi.org/10.1016/j.buildenv.2020.107370.

[3] G.X. Zhu, W. Zhu, Y. Lou, J. Ma, W.Q. Yao, R.L. Zong, Y.F. Zhu, Encapsulate α-MnO_2 nanofiber within graphene layer to tune surface electronic structure for efficient ozone decomposition, Nat. Commun. 12 (2021) 4152, https://doi.org/10.1038/s41467-021-24424-x.

[4] J. Li, J. Huang, R. Cao, P. Yin, L.J. Wang, Y. Liu, X.C. Pan, G.X. Li, M.G. Zhou, The association between ozone and years of life lost from stroke, 2013–2017: a retrospective regression analysis in 48 major Chinese cities, J. Hazard. Mater. 405 (2021), 124220, https://doi.org/10.1016/j.jhazmat.2020.124220.

[5] P.F. Liu, H.Q. Song, T.H. Wang, F. Wang, X.Y. Li, C.H. Miao, H.P. Zhao, Effects of meteorological conditions and anthropogenic precursors on ground-level ozone concentrations in Chinese cities, Environ. Pollut. 262 (2020), 114366, https://doi.org/10.1016/j.envpol.2020.114366.

[6] M.Y. Lin, L.W. Horowitz, Y.Y. Xie, F. Paulot, S. Malyshev, E. Shevliakova, A. Finco, G. Gerosa, D. Kubistin, K. Pilegaard, Vegetation feedbacks during drought exacerbate ozone air pollution extremes in Europe, Nat. Clim. Change 10 (2020) 444–451, https://doi.org/10.1038/s41558-020-0743-y.

[7] M.L. Ma, G.B. Yao, J.P. Guo, K.X. Bai, Distinct spatiotemporal variation patterns of surface ozone in China due to diverse influential factors, J. Environ. Manag. 288 (2021), 112368, https://doi.org/10.1016/j.jenvman.2021.112368.

[8] X. Lu, X.P. Ye, M. Zhou, Y.H. Zhao, H.J. Weng, H. Kong, K. Li, M. Gao, B. Zheng, J. T. Lin, F. Zhou, Q. Zhang, D.M. Wu, L. Zhang, Y.H. Zhang, The underappreciated role of agricultural soil nitrogen oxide emissions in ozone pollution regulation in North China, Nat. Commun. 12 (2021), 5021, https://doi.org/10.1038/s41467-021-25147-9.

[9] L.F. Yang, Z.B. Yuan, H.H. Luo, Y.R. Wang, Y.Q. Xu, Y.S. Duan, Q.Y. Fu, Identification of long-term evolution of ozone sensitivity to precursors based on two-dimensional mutual verification, Sci. Total Environ. 760 (2021), 143401, https://doi.org/10.1016/j.scitotenv.2020.143401.

[10] J. Sun, Z.X. Shen, R.N. Wang, G.H. Li, Y. Zhang, B. Zhang, K. He, Z.Y. Tang, H. M. Xu, L.L. Qu, S.S.H. Ho, S.X. Liu, J.J. Cao, A comprehensive study on ozone pollution in a megacity in North China Plain during summertime: observations, source attributions and ozone sensitivity, Environ. Int. 146 (2021), 106279, https://doi.org/10.1016/j.envint.2020.106279.

[11] W.J. Yang, J.N. Ren, J.J. Li, H.W. Zhang, K. Ma, Q.W. Wang, Z.Y. Gao, C.C. Wu, I. D. Gates, A novel Fe-Co double-atom catalyst with high low-temperature activity and strong water-resistant for O_3 decomposition: a theoretical exploration, J. Hazard. Mater. 421 (2022), 126639, https://doi.org/10.1016/j.jhazmat.2021.126639.

[12] J.M. Ma, R.N. Cao, Y.L. Dang, J.L. Wang, A recent progress of room–temperature airborne ozone decomposition catalysts, Chin. Chem. Lett. 32 (2021) 2985–2993, https://doi.org/10.1016/j.cclet.2021.03.031.

[13] J.Z. Ma, X.T. Li, C.B. Zhang, Q.X. Ma, H. He, Novel $CeMn_aO_x$ catalyst for highly efficient catalytic decomposition of ozone, Appl. Catal. B-Environ. 264 (2020), 118498, https://doi.org/10.1016/j.apcatb.2019.118498.

[14] Z.S. Wang, Y.F. Chen, X.T. Li, G.Z. He, J.Z. Ma, H. He, Layered double hydroxide catalysts for ozone decomposition: the synergic role of M^{2+} and M^{3+}, Environ. Sci. Technol. 56 (2022) 1386–1394, https://doi.org/10.1021/acs.est.1c07829.
[15] A.Q. Wang, J. Guan, L. Zhang, H. Wang, G.J. Ma, G.J. Fan, W.X. Tang, N. Han, Y. F. Chen, In situ synthesis of monolithic Cu_2O–CuO/Cu catalysts for effective ozone decomposition, J. Phys. Chem. C 126 (2022) 317–325, https://doi.org/10.1021/acs.jpcc.1c10208.
[16] X.S. Liang, L.S. Wang, T.C. Wen, H.J. Liu, J. Zhang, Z. Liu, C.Z. Zhu, C. Long, Mesoporous poorly crystalline α-Fe_2O_3 with abundant oxygen vacancies and acid sites for ozone decomposition, Sci. Total Environ. 804 (2022), 150161, https://doi.org/10.1016/j.scitotenv.2021.150161.
[17] J.Y. Ding, F. Cheng, Z. Meng, Y. Cao, F.N. Han, D.B. Chen, M.X. Cao, G.L. Zhang, J. H. Kang, S.X. Xu, Q. Xu, Core-shell-Like structured Co_3O_4@SiO_2 catalyst for highly efficient catalytic elimination of ozone, Front. Chem. 9 (2021), 803464, https://doi.org/10.3389/fchem.2021.803464.
[18] S.Y. Gong, A.Q. Wang, Y. Wang, H.D. Liu, N. Han, Y.F. Chen, Heterostructured Ni/NiO nanocatalysts for ozone decomposition, ACS Appl. Nano Mater. 3 (2020) 597–607, https://doi.org/10.1021/acsanm.9b02143.
[19] H.K. Song, L.L. Xu, M.D. Chen, Y. Cui, C.E. Cui, J. Qiu, L. Xu, G. Cheng, X. Hu, Recent progresses in the synthesis of MnO_2 nanowire and its application in environmental catalysis, RSC Adv. 11 (2021) 35494–35513, https://doi.org/10.1039/d1ra06497e.
[20] X.T. Li, J.Z. Ma, H. He, Recent advances in catalytic decomposition of ozone, J. Environ. Sci. 94 (2020) 14–31, https://doi.org/10.1016/j.jes.2020.03.058.
[21] B. Dhandapani, S.T. Oyama, Gas phase ozone decomposition catalysts, Appl. Catal. B-Environ. 11 (1997) 129–166, https://doi.org/10.1016/s0926-3373(96)00044-6.
[22] L. Zhang, J.W. Yang, A.Q. Wang, S.H. Chai, J. Guan, L.F. Nie, G.J. Fan, N. Han, Y. F. Chen, High performance ozone decomposition spinel $(Mn,Co)_3O_4$ catalyst accelerating the rate-determining step, Appl. Catal. B-Environ. 303 (2022), 120927, https://doi.org/10.1016/j.apcatb.2021.120927.
[23] G. Abdallah, R. Bitar, S.K.P. Veerapandian, J.M. Giraudon, N.D. Geyter, R. Morent, J.F. Lamonier, Acid treated Ce modified birnessite–type MnO_2 for ozone decomposition at low temperature: effect of nitrogen containing co-pollutants and water, Appl. Surf. Sci. 571 (2022), 151240, https://doi.org/10.1016/j.apsusc.2021.151240.
[24] Z.B. Sun, Y.N. Si, S.N. Zhao, Q.Y. Wang, S.Q. Zang, Ozone decomposition by a manganese-organic framework over the entire humidity range, J. Am. Chem. Soc. 143 (2021) 5150–5157, https://doi.org/10.1021/jacs.1c01027.
[25] X. Chen, Q.Q. Xu, Y. Zhou, Q.L. Zhu, H.F. Huang, Z.Y. Pan, P.F. Zhang, S. Dai, H. F. Lu, Facile and flexible preparation of highly active CuCe monolithic catalysts for VOCs combustion, ChemistrySelect 2 (2017) 9069–9073, https://doi.org/10.1002/slct.201701850.
[26] X. Chen, Z.L. Zhao, Y. Zhou, Q.L. Zhu, Z.Y. Pan, H.F. Lu, A facile route for spraying preparation of Pt/TiO_2 monolithic catalysts toward VOCs combustion, Appl. Catal. A-Gen. 566 (2018) 190–199, https://doi.org/10.1016/j.apcata.2018.08.025.
[27] X.F. Yan, W.G. Gao, W.S. Mao, W. Na, H.H. Huo, S. Chang, Preparation of Cu-ZnO-ZrO_2 catalyst by sol-gel method: effect of citric acid content on catalyst performance, Chem. Ind. Eng. Prog. 39 (2020) 4032–4040, https://doi.org/10.16085/j.issn.1000-6613.2019-2051.
[28] R. Roknabadi, A.A. Mirzaei, H. Atashi, Assessment of composition and calcination parameters in Fischer-Tropsch synthesis over Fe–Mn–Ce/γ-Al_2O_3 nanocatalyst, Oil Gas. Sci. Technol. 76 (2021) 4032–4040, https://doi.org/10.2516/ogst/2020089.
[29] K.H. Wu, T.H. Ting, M.C. Li, W.D. Ho, Sol–gel auto-combustion synthesis of SiO_2-doped NiZn ferrite by using various fuels, J. Magn. Magn. Mater. 298 (2006) 25–32, https://doi.org/10.1016/j.jmmm.2005.03.008.
[30] R.J. Zhang, J.J. Huanag, J.T. Zhao, Z.Q. Sun, Y. Wang, Sol−gel auto-combustion synthesis of zinc ferrite for moderate temperature desulfurization, Energy Fuels 21 (2007) 2682–2687, https://doi.org/10.1021/ef070064w.
[31] A.M. El-hadi, H.R. Alamri, The new generation from biomembrane with green technologies for wastewater treatment, Polymers 10 (2018) 1174, https://doi.org/10.3390/polym10101174.
[32] S. Dey, S. Sarkar, H. Paul, E. Zangrando, P. Chattopadhyay, Copper(II) complex with tridentate N donor ligand: synthesis, crystal structure, reactivity and DNA binding study, Polyhedron 29 (2010) 1583–1587, https://doi.org/10.1016/j.poly.2010.01.022.
[33] J.T. Kloprogge, D. Wharton, L. Hickey, R.L. Frost, Infrared and Raman study of interlayer anions CO_3^{2-}, NO_3^-, SO_4^{2-} and ClO_4^- in Mg/Al-hydrotalcite, Am. Mineral. 87 (2002) 623–629, https://doi.org/10.2138/am-2002-5-604.
[34] A. Mali, A. Ataie, Structural characterization of nano-crystalline BaFe12O19 powders synthesized by sol–gel combustion route, Scr. Mater. 53 (2005) 1065–1070, https://doi.org/10.1016/j.scriptamat.2005.06.037.
[35] L. Nalbandian, A. Evdou, C. Matsouka, V. Zaspalis, Assessment of $(La_{1-x}Sr_x)MnO_{3\pm\delta}$ perovskites as oxygen-carrier materials in chemical-looping processes, Fuel Process. Technol. 226 (2022), 107086, https://doi.org/10.1016/j.fuproc.2021.107086.
[36] P. Chen, F. Dong, M.X. Ran, J.R. Li, Synergistic photo-thermal catalytic NO purification of MnO_x/g-C_3N_4: enhanced performance and reaction mechanism, Chin. J. Catal. 39 (2018) 619–629, https://doi.org/10.1016/S1872-2067(18)63029-3.
[37] Z.H. Lian, J.Z. Ma, H. He, Decomposition of high-level ozone under high humidity over Mn–Fe catalyst: the influence of iron precursors, Catal. Commun. 59 (2015) 156–160, https://doi.org/10.1016/j.catcom.2014.10.005.
[38] Z.M. Chan, D.A. Kitchaev, J.N. Weker, C. Schnedermann, K. Lim, G. Ceder, W. Tumas, M.F. Toney, D.G. Nocera, Electrochemical trapping of metastable Mn^{3+} ions for activation of MnO_2 oxygen evolution catalysts, Proc. Natl. Acad. Sci. USA 115 (2018) E5261–E5268, https://doi.org/10.1073/pnas.1722235115.
[39] X.T. Li, J.Z. Ma, C.B. Zhang, R.D. Zhang, H. He, Detrimental role of residual surface acid ions on ozone decomposition over Ce-modified γ-MnO_2 under humid conditions, J. Environ. Sci. 91 (2020) 43–53, https://doi.org/10.1016/j.jes.2019.12.004.
[40] L.G. Tao, G.F. Zhao, P.J. Chen, Z.Q. Zhang, Y. Liu, Y. Lu, High-performance Co-MnO_x composite oxide catalyst structured onto Al-fiber felt for high-throughput O_3 decomposition, ChemCatChem 11 (2019) 1131–1142, https://doi.org/10.1002/cctc.201801401.
[41] Y. Rao, D.B. Zeng, X.Z. Cao, G.W. Qin, S. Li, Synthesis of doped MnO_x/diatomite composites for catalyzing ozone decomposition, Ceram. Int. 45 (2019) 6966–6971, https://doi.org/10.1016/j.ceramint.2018.12.195.
[42] Y. Liu, P.Y. Zhang, Catalytic decomposition of gaseous ozone over todorokite-type manganese dioxides at room temperature: effects of cerium modification, Appl. Catal. A-Gen. 530 (2017) 102–110, https://doi.org/10.1016/j.apcata.2016.11.028.
[43] T. Batakliev, G. Tyuliev, V. Georgiev, M. Anachkov, A. Eliyas, S. Rakovsky, Ozone decomposition reaction over α-alumina-supported silver catalyst: comparative study of catalytic surface reactivity, Ozone-Sci. Eng. 37 (2015) 216–220, https://doi.org/10.1080/01919512.2014.957261.